European Polymer Journal 61 (2014) 172–185

Contents lists available at ScienceDirect

European Polymer Journal

journal homepage: www.elsevier.com/locate/europolj

Macromolecular Nanotechnology

On the packing and the orientation of P(NDI2OD-T2) at low molecular weight

W. Porzio [a,*], G. Scavia [a], L. Barba [b], G. Arrighetti [b], C.R. McNeill [c]

[a] Istituto per lo studio delle Macromolecole del CNR, via E. Bassini 15, 20133 Milano, Italy
[b] Istituto di Cristallografia-Sincrotrone Elettra, Strada Statale 14-Km 163,5 Area Science Park, 34149 Basovizza, Trieste, Italy
[c] Department of Materials Engineering, Faculty of Engineering, Monash University, Clayton, VIC 3800, Australia

ARTICLE INFO

Article history:
Received 24 July 2014
Received in revised form 26 September 2014
Accepted 11 October 2014
Available online 22 October 2014

Keywords:
Crystal structure
Microstructure
Macromolecule orientation
Intensity comparison

ABSTRACT

A detailed structural and orientational study on thin films of poly([n,n′-bis(2-octyldodecyl)-11naphthalene-1,4,5,8-bis(dicarboximide)-2,6-diyl]-*alt*-5,5′-(2,2′-12 bithiophene)) (**P(NDI2OD-T2)**) with low molecular weight is reported. The combination of grazing incidence diffraction with varied depth sensitivity and powder diffraction using synchrotron radiation provide new insights on the unit cell, confirming polymorphic behavior, and configuration ratio, i.e. *face-* versus *edge-on*. The effect of thermal treatment on microstructure is also presented. Insights of the macromolecule configuration, specifically the reciprocal position of bis-dicarboximide and bi-thiophene residues, are derived from simulation of 2D images based on reliable models.

Published by Elsevier Ltd.

1. Introduction

Efforts to produce materials suitable for high-performance ambipolar organic field effect transistors (OFETs) [1–4] and organic photovoltaic cells (OPVs) [5–7] have received renewed attention especially using π-conjugated polymers. Materials based on the naphthalene-dicarboximide moiety (**NDI2OD**) in particular have attracted much interest, with the polymer poly([n,n′-bis(2-octyldodecyl)-11naphthalene-1,4,5,8-bis(dicarboximide)-2,6-diyl]-*alt*-5,5′-(2,2′-12 bithiophene)) (**P(NDI2OD-T2)**), representing a prototypical case [8–18] (see Fig. 1). Indeed, OFET devices based on this polymer exhibit excellent performances irrespectively of the processing conditions [8,13,19]. Moreover encouraging performances in OPV devices in blends with suitable donor polymers have been presented [14,15].

On the other hand, such a complex system displays a value of activation energy or trap depth, evaluated from temperature dependent FET measurements, typical of a well ordered material, as reported in Ref. [20].

Previous studies [8,10–12,14–21] have addressed most of the features responsible for the remarkable performance of this material by using both grazing incidence wide angle X-ray scattering (GIWAXS) and high resolution electronic microscopy. In fact, GIWAXS on thick films [10] and HRTEM on thin films (20 nm thick) [21] showed that **P(NDI2OD-T2)** chains pack in crystalline lamellae with a tendency to orient flat onto the substrate, wherein macromolecules run with tiles of N,N′-bis(2-octyldodecyl)-11naphthalene-1,4,5,8-bis(dicarboximide) (**NDI2OD**) facing onto the substrate.

The thermal treatment at 330 °C melts the polymer crystallites and the subsequent slow cooling provokes a configuration change, i.e. from *face-on* to *edge-on* orientations, with the high electron mobility unexpectedly maintained in top-gate OFETs [8]. In fact the exhaustive study of Rivnay et al. [12] was not able to disentangle the different factors contributing to the persistence of a large electron mobility in FET devices after melt annealing. More recently

* Corresponding author. Tel.: +39 0223699371; fax: +39 0270636400.
E-mail address: w.porzio@ismac.cnr.it (W. Porzio).

http://dx.doi.org/10.1016/j.eurpolymj.2014.10.005
0014-3057/Published by Elsevier Ltd.

a significant electron mobility anisotropy was detected in rubbed films for charge transport parallel and perpendicular to the rubbing direction [19].

Both the NEXAFS study of Schuettfort et al. [17] on thick films and microscopic study (HRTEM and STEM) of Takacs et al. [21] addressed part of these apparent contradictions, describing ample crystallinity increased under appropriate thermal treatments; preferential *edge-on* orientations of macromolecules close to the air-interface and conversely *flat-on* orientations in the bulk; influence of different substrates on the orientations at substrate–layer interface; lamella rotation upon melt annealing, and consequent large *edge-on* conversion of the main-chains; finally detection of macromolecules oriented neither *edge-* nor *face-*on interpreted as an effect of local conformational disorder [17,21].

The prevailing *edge-on* orientation close to the active region in OFET devices together with the complex nanoscale organization account for large electron mobility either in-plane [22] or out-of plane [12,19]. A further complication arises from the polymorphism observed by Brinkmann [16,19] and addressed according to film thermal treatment towards a specific phase (hereinafter labeled ***1*** or ***2***).

Moreover a recent paper of Steyrleuthner et al. pointed out the relevant role of regioregularity in addressing both polymer crystallinity and molecular orientation [23] which was confirmed as being important in determining electron mobility as measured in electron-only diodes.

None the less, the lack of stereoselectivity in the synthetic approach allows the co-presence of different configurations along with the macromolecule, clearly envisaged by Lemaur et al. [24]. The situations differ by the reciprocal position of thiophenic sulphur with respect to **NDI2OD** oxygen atoms, namely three cases can occur SYN–SYN (**S**), SYN–ANTI (**SA**), and ANTI–ANTI (**A**) which are sketched in Scheme 1 and detailed in Section 3.4. Such a complication can produce mis-match or meandering of polymeric backbones [21], together with a slight d-spacing increase [23].

This complex scenario necessitates, in our opinion, a further study using a low molecular weight (M_n) material considering:

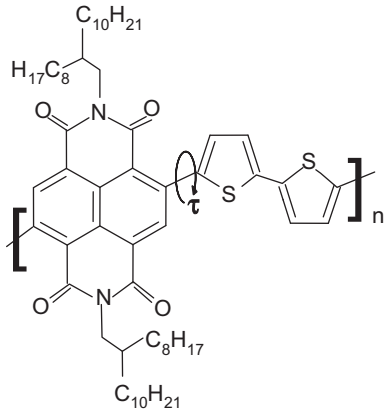

Fig. 1. Scheme of (**P**(**NDI2OD-T2**)) evidencing torsion angle τ between **NDI2OD** and **T2** moieties.

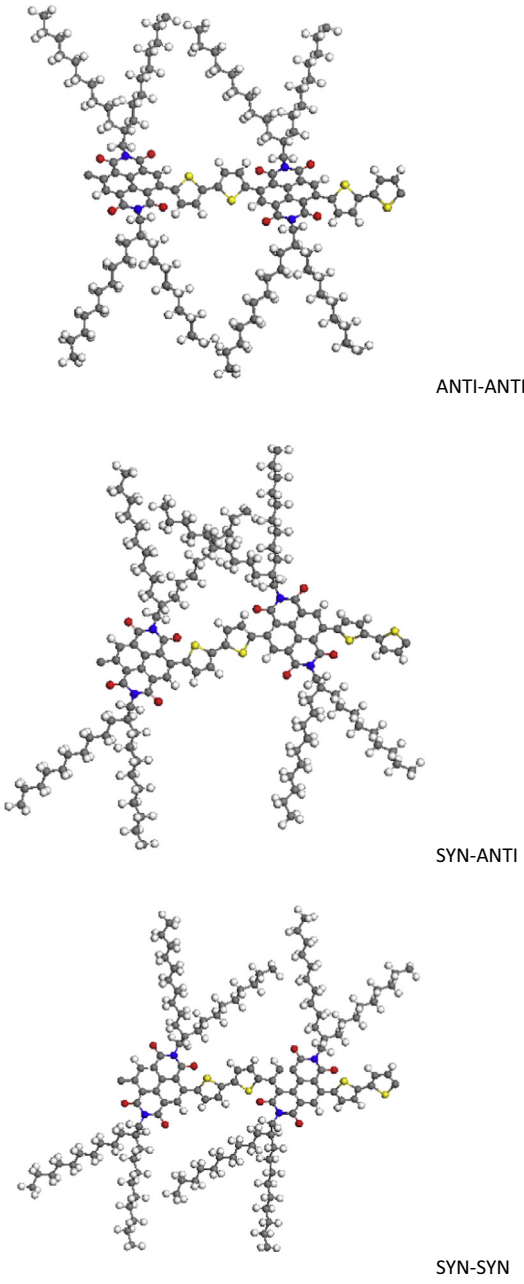

Scheme 1.

- The effect of M_n and its polydispersivity (PDI); the afore-mentioned studies employed polymer batches of 25KD or 33KD and PDI over 3.0, hence the possibility of local disorder. Chain mis-overlapping, has to be prevented by lowering values of these parameters.
- The thickness effect -bulk-effect- which increases local disorder, mis-orientation and crystallite size reduction; although the charge mobility in FET devices is prevailing in the first layers [25] the bulk-layer situation can influence their local order/orientation.

– The possible configuration (**S**, **SA**, **A**) of **T2** versus **NDI2OD** moieties with respect to the substrate, as exemplified in Scheme 2 [11,21], even displaying different length, conformation, and energy [17,21,26], should be accounted for while simulating reliable crystal packing to be compared with the experimental data.

We tried to address these issues by combining depth resolved analysis in ultra-thin films using GIWAXS techniques [27], in combination with X-ray diffraction of annealed powders and 2D image simulation employing models from crystallographic information files (CIF) built up in different conformations, crystal symmetry, and packing.

2. Experimental

P(**NDI2OD-T2**) was supplied by Polyera Corp. (ActivInk N2200) with the average molecular weight (M_n) and polydispersity index (PDI) determined from GPC analysis. GPC analysis was corrected by a procedure based on SEC calibration using **NDI2OD-T2** oligomers [28] and by comparing the results of NMR analysis of end chains [16]. Different spin-coated samples were obtained by spinning from di-chlorobenzene solutions, onto 700 μm thick silicon wafers covered with 300 nm SiO_2. All substrates were cleaned by ultrasonication in acetone, then in propanol, and finally subjected to 10 min of oxygen plasma treatment. Subsequently silanization using either hexamethyldisilazane (HMDS) or octadecyltrichlorosilane (OTS) was performed according to the conditions detailed in Ref. [27].

In Table 1 polymer characteristics, preparation conditions and thermal treatments are reported. Such conditions were properly chosen in order to minimize film roughness and thickness.

Thermal treatment was performed on a hot-stage with temperature control better than 0.05 °C under N_2 flux (O_2 residual less than 0.5 p.p.m.). Samples were heated at two temperatures: 230°, to allow side-chain crystallization, without any phase transition, and 330°, well above the melting point to cancel memory of any previous material ordering; waiting for 40 min, then slowly cooled to 30 °C at a rate of 0.1 °C/min.

GIWAXS measurements were performed at the X-ray Diffraction beamline 5.2 at the Synchrotron Radiation Facility Elettra in Trieste (Italy). The X-ray beam emitted by the wiggler source on the Elettra 2 GeV electron storage ring was monochromatized by a Si(1 1 1) double crystal monochromator, focused on the sample and collimated by a double set of slits giving a spot size of 0.2 × 0.2 mm. The beam was monochromatized at energies ranging from 8 keV up to 12.4 keV. The samples were oriented by means of a four-circle diffractometer with a motorized goniometric head. The X-ray beam direction was fixed, while the sample holder could be rotated about the different diffractometer axes, in order to reach the sample surface alignment in the horizontal plane containing the X-ray beam by means of laser light reflection. Subsequently it was possible to rotate the sample around an axis perpendicular to this plane or, alternatively, vary the angle between beam and surface (angle of incidence). Bidimensional diffraction patterns were recorded with either a 2 M Pilatus silicon pixel X-ray detector (DECTRIS Ltd., Baden, Switzerland) or CCD camera (MAR research) of 165 mm diameter (both positioned perpendicular to the incident beam, at a variable distance, 133 up to 200 mm distance from the sample), to record the diffraction patterns in reflection mode. Sample and detector were kept fixed during the measurements.

In the reported data, the sample inclination to the beam was changed from $\omega = -0.05°$ to $\omega = 0.25°$, in steps of 0.05° to allow penetration depth all along the thickness [29], yielding seven diffraction images (see Fig. S1 in Supplementary data for details). The q resolution of 2D images collected was estimated by means of Lanthanum hexaboride powder (standard reference material 660a of NIST) and it has been evaluated ranging from 0.2 to 0.3 nm^{-1} both for Q_z and Q_{xy}, in agreement with other synchrotron measurements [30,31].

The same calibration standard allowed for the integration of 2D patterns using the software Fit2D [32] yielding several series of powder-like patterns, corrected for geometry, Lorentz, and beam polarization effects.

Peaks positions were extracted by means of the program Winplotr [33]. CIF files for simulation of 2D patterns were obtained from MATSTUDIO package [34].

NEXAFS spectroscopy was performed at the soft X-ray beamline at the Australian Synchrotron. The TEY signal was recorded via the drain current through the sample with electron yield signals normalized to the incident photon flux using the "stable monitor method" [17]. The tilt angles were determined by fitting Gaussian peaks to the 4 π^* peaks in the π^* manifold, plotting the sum of the area of these four peaks vs the X-ray angle of incidence and fitting to Eq. (9.16) of Stöhr [35]. Further details can be found in previous publications [17].

Table 1
Films characteristics.

Sample	M_n[a]	PDI[a]	Conc[b]	Spin speed[c]	Thickness[d]	Annealing T[e]
I	11,000	1.5	6–10	2000–3000	10–20	230° and 330°
II	33,000	2.0	8–15	2000–3000	10–20	230° and 330°
III	25,000	4.0	20	2500–3000	50	230° and 330°

[a] Derived from SEC analysis; the value was corrected according to the procedure indicated in Refs. [16,28].
[b] mg cm^{-3} dichlorobenzene solution under N_2 atmosphere.
[c] Revolutions per minute at 25 °C.
[d] As determined by AFM analysis, average values on ten samples, e.s.d. 2 nm.
[e] Thermal treatment was carried out as described in the text.

3. Results and discussion

3.1. General considerations

With the exception of the recent paper of Takacs et al. [21] that reported on 20 nm thick films of **P(NDI2OD-T2)** with medium M_n and high PDI, previous studies were performed on films of large thickness (50–100 nm) [8–17]. In this kind of samples *bulk-effect* tangles the study of the configurations close to the substrate-polymer interface. In fact, increased thickness leads to an augment in both the amorphous component and mis-orientation along with direction normal to the film and the reduction of crystallite dimension [27]. Moreover the use of high M_n material, i.e. 300 kD [8,10,12], introduces the further complication of in-chain defects and entanglements. Finally the relatively high PDI (e.g. larger than 3–4) makes chain-folding easier, leads to the formation of local disordered regions, and results in reduced long-range order.

Therefore we examined films of small/medium M_n and PDI polymers, namely 11KD/33KD and 1.8/2.2, labeled type **I** and **II** respectively (see Table 1). After applying the proper corrections according to Refs. [15,28], we estimated a polymerization degree of 10 and 30 units, corresponding to an average chain length of 14 nm and 45 nm respectively, while for type **III** films based on a batch with medium M_n and large PDI such a correction was not applied, taking the values from the literature [16]. In addition, better surface homogeneity (namely a roughness less than 3 nm by AFM analysis) is achieved limiting the thickness to less than 12 nm.

The small M_n polymer is particularly interesting in view of the absence of folding, therefore aiding the crystallisation/orientation in spite of the lack of strongly orienting substrate [16,19], as recently reviewed by Brinkmann [36] and demonstrated by Kohn et al. [37] in case of blend of poly(3-hexylthiophene) **P3HT** and ([6,6]-phenyl-C61-butyric acid methyl ester). Moreover this M_n range could reduce the meandering of backbone as shown in larger M_n materials [21].

Optimal conditions to evidence fine differences along the thickness in variously treated films together with diffraction data treatment are reported in Supplementary data.

In particular, GIWAXS data from films of different polymeric systems, namely polyimide [38], **P3HT** [27,39], poly(9,9-di-*n*-octylfluorene-*alt*-benzothiadiazole) [40], and poly(2,5-bis(3-tetradecylthiophen-2-yl)thieno [3,2-b]thiophene) [41] indicate that below and over the critical incidence angle the patterns significantly differ allowing for determination of crystallite perfection and dimensions and orientation (see below).

To independently check the surface orientation of the macromolecules even in the amorphous part [17], NEXAFS spectroscopy was carried out onto selected films, the results obtained from data collected in total electron yield (TEY) mode together with the original diagrams are displayed in Supplementary data. Such a mode permits a surface sensitivity of 3 nm, i.e. the last layers of thin films. The average tilt angle of the conjugated backbone is measured with respect to the surface normal, with the C1s to π^* transition dipole moment (TDM) perpendicular to conjugated ring planes. So for perfect *edge-on* to the substrate $\langle\gamma\rangle$ would be 90° and for perfect *face-on* to the substrate $\langle\gamma\rangle$ would be 0°. Of course even in the case of quite thin films, the surface molecular orientation may not match the bulk/interface molecular orientation [17].

In all reported cases, $\langle\gamma\rangle$ of the effective C1s to π^* TDM of the polymer repeat unit is greater than 45°, and more interestingly significantly larger than magic angle 54.7°, which could correspond to a random distribution of tilt angles rather than an actual orientational preference. Hence, consistently in agreement with results of Ref. [17], all films show a preferential *edge-on* molecular orientation at the top surface, as expected.

For each sample, the parameters evaluated are: the size of crystallite along with different crystallographic directions (CD) expressed with average L_{hkl} (nm), the perfection of crystallites according to Hosemann paracrystal model [42] given by lattice fluctuation factor $g_{(hkl)} = (\bar{d}^2_{(hkl)}/\bar{d}_{(hkl)}{}^2 - 1)^{1/2}$, indicating the standard deviation of $d_{(hkl)}$ [27,29,42–44] evaluated over more orders of CD, and non uniform strain $\varepsilon_{rms} = (\langle e^2\rangle)^{1/2}$, where $e = \delta d_{(hkl)}/d_{(hkl)}$, defined as root mean square of the lattice variations in the sample [30,45].

Table S1 shows the *d*-spacing of the cell axis, while in Fig. 2 2D images of type **I** films prepared on bare Silicon, onto HMDS, and onto OTS and annealed at 230 °C are presented, along with the extracted IP and OP profiles. Table 2 presents the above-described physical quantities for films annealed at 230 °C extracted from in-plane (IP) profiles while Table 3 shows these quantities as extracted from out-of-plane (OP) profiles. Tables 2 and 3 tabulate data not only for type **I** films (2D images shown in Fig. 2) but also for type **II** films (2D images shown in Fig. 3) and type **III** films (2D images shown in Fig. S2).

Fig. 2 experimental two dimensional GIXS patterns of **P(NDI2OD-T2)** type **I** films onto bare Si, HMDS, and OTS annealed at 230 °C recorded at $\alpha_i = 0.2°$. Approximate Q_{xy} and Q_z scales provided to allow comparison with OP-blue- and IP-grey-profiles extracted from the images, properly scaled and shifted for clarity, reported in *Q*-scale. The X-ray wavelength is 0.12 nm.

3.2. Main features

Fig. 2 shows that irrespective of both the deposition conditions and the thermal history, arcs at $q = 0.25$ A^{-1}, attributed to (100), are present, indicating multiple crystallite orientations, as observed in previous studies, even in greater extent for larger M_n polymers [10,11]. Only after adequate thermal treatment over 330 °C does the reflection intensity significantly decrease, although not completely, as expected. This observation strongly suggests that even in thin films (10 nm thick) some mis-oriented lamellae are present. As a comparison, in Fig. 3 2D images of type **I** films of polymer treated at 330 °C, and related profiles IP and OP are presented.

The amorphous component, observed at 1.4 A^{-1}, is generally small if incidence angles are less than 0.15° (see Fig. S3 in Supplementary data) thus excluding diffraction SiOx amorphous substrate [27,37], as reported by Schuettfort et al.[17] and also by Steyrleuthner et al. [46]. As a

Table 2
Crystallite size, g-factors, and d-spacing derived from in-plane profiles of 2D images of selected thin films annealed at 230 °C of **P**(**NDI2OD-T2**) onto different self-assembled monolayers (SAM) covering Si substrate.

SAM[a]	Profile IP									
	$L_{[100]}$ [c]	$g_{[100]}$ [d] 100/200	$g_{[100]}^{200/300}$	$g_{[100]}^{300/400}$	ε_{rms} [e]	$d_{[001]}$ [b]	$L_{[001]}$ [c]	$g_{[001]}^{001/002}$	$g_{[001]}^{002/004}$	ε_{rms}
I 10K Si 230[f]	25	3.3	3.0		1.4	1.4	12	2.5	2.5	0.9
I 10KHMDS 230	25	4.3	1.8	1.6	1.3	1.405	11	2.5	3.1	0.8
I 10K OTS 230	26	4			1.6	1.395	12			
II 30K Si 230	17	3.4	3.6	2.1	1.7	1.40	18	2.5	2.7	1.2
II 30HMDS 230	20	5.3	3.4	3.6	2.2	1.395	16	2.3	4.0	1.1
II 30K OTS 230	20	5	3.3	2.2	1.8	1.41	18		5.1	1.1
III Si 230	19	5.7	3.	3.6	2.0	1.39	10.5	2.5	4.6	1.4
III OTS 230	21	6.4	3.3	2.5	2.2	1.4	12.5	2.4	5	1.9

[a] The three issues indicate the M_n, the film substrate and the annealing temperature respectively, see text. The values of L and d are in nm, while g and ε are %. The M_n has been determined with correction using Ref. [28] (see text for the values).
[b] All the spacing are not corrected for refraction effects in view of negligible value calculated ($\sim 10^{-4}$).
[c] L is the average crystallite dimension as derived from Refs. [27,45]. The estimated standard deviation (e.s.d.) is $\sim$1 nm.
[d] g_{hkl} is the lattice fluctuation factor according to Hosemann paracrystal theory, calculated over closest order (1–2, 2–3 etc).
[e] ε_{rms} is the non uniform strain (%) which e.s.d. is 0.25.
[f] The incidence angle is 0.15° or in some cases 0.2° As the critical angle is close to 0.135° the penetration depth is well over the organic layer thickness.

Table 3
Crystallite size, g-factors, and d-spacing derived from out-of-plane profiles of 2D images of selected thin films annealed at 230 °C of **P**(**NDI2OD-T2**) onto different self-assembled monolayers (SAM) covering Si substrate.

SAM[a]	Profile OP						
	$L_{(100)}$ [c]	$g_{[100]}$ [d] 100/200	$g_{[100]}$ 200/300	$g_{[100]}^{200/300}$	ε_{rms} [e]	$d_{[020]}$ [b]	$L_{[020]}$ [c]
I 10K Si 230[f]	12	3.35	3.35		2.5	0.382	10
I 10KHMDS 230	25	4.3	2.6	2.5	1.9	0.384	3.5
I 10K OTS 230	15	2.7	3.3		1.6	0.378	4
II 30K Si 230	9.5	5	4.2		3.2	0.385	5
II 30 HMDS 230	10					0.389	3.5
II 30K OTS 230	10	4.85	4.05		3.4	0.387	4
III Si 230	10					0.382	4.
III OTS 230	9	6.8	4.3	4.4		0.388	4

[a] The three issues indicate the M_n, the film substrate and the annealing temperature respectively, see text. The values of L and d are in nm, while g and ε are %. The M_n has been determined with correction using Ref. [28] (see text for the values).
[b] All the spacing are not corrected for refraction effects in view of negligible value calculated ($\sim 10^{-4}$).
[c] L is the average crystallite dimension as derived from Refs. [27,45]. The estimated standard deviation (e.s.d.) is $\sim$1 nm.
[d] g_{hkl} is the lattice fluctuation factor according to Hosemann paracrystal theory, calculated over closest order (1–2, 2–3 etc).
[e] ε_{rms} is the non uniform strain (%) which e.s.d. is 0.25.
[f] The incidence angle is 0.15° or in some cases 0.2° As the critical angle is close to 0.135° the penetration depth is well over the organic layer thickness.

matter of fact, thin films of **P**(**NDI2OD-T2**) display high crystallinity [21]. The second evidence consists in the slight shortening of the *a* axis in type **I** films as compared with the corresponding type **II** samples and also with the previously reported values [11,12,17]-only in Ref. [11] similar values were reported- for films obtained from larger M_n polymer batches, both in IP and in OP profiles (see Table S1) [47]. Specifically the $d_{(100)}$ values derived in Refs. [9,10,17,23,30] range from 2.45 to 2.5 nm and are larger than the averaged value derived from the IP profiles of most crystallized films (2.4 nm, see Table S1). An even more pronounced contraction for all samples is observed in the (020) reflection, whose *d*-spacing is close to 0.39 nm, consistently smaller than the values observed in other films [11,12,16], which span from 0.392 to 0.4 nm. In fact, from OP profiles shown in Fig. 3, a spacings of 0.389 nm -attributed to (0 2 0)- is derived. These observations clearly indicate that for type **I** films (see Table 1) a closer packing is achieved.

It should be noted that for the case of films, obtained by both casting or spin coating having thickness larger than 25 nm, some double arcs are recognizable in 2D images, yielding a range of values for both [020] and for [004]. This observation suggests a separate crystallisation of lamellae mis-oriented with respect to the substrate all along the thickness (see Fig. S4 in Supplementary data).

Concerning the crystallite dimensions and their perfection, expressed by L_{hkl} and g_{hkl} respectively, type **I** films display, in general, slightly larger L_{hkl} values and shorter g_{hkl} as well as ε_{rms} values, if compared with type **II** films -larger M_n-, which 2D patterns together with extracted profiles are shown in Fig. 4 – and also with the optimized films reported in Ref. [30]. As an example, lines 3 to 5 of Table 2 and line 4 of Table 3 are fully in agreement with these observations.

The range order reduction even after proper thermal treatment for type **III** films is significantly detected (see 2D images and extracted profiles in Fig. S2).

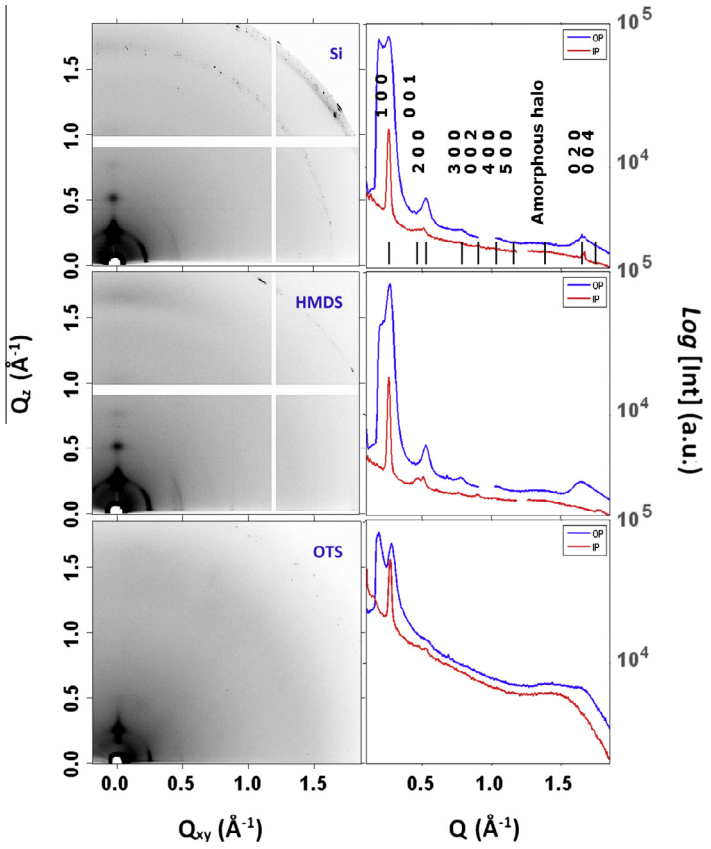

Fig. 2. Experimental two dimensional GIXS patterns of **P**(**NDI2OD-T2**) type **I** films onto bare Si, HMDS, and OTS annealed at 230 °C recorded at $\alpha_i = 0.2°$. Approximate Q_{xy} and Q_z scales provided to allow comparison with OP-blue- and IP-grey-profiles extracted from the images, properly scaled and shifted for clarity, reported in Q-scale. The X-ray wavelength is 0.12 nm. (For interpretation of the references to color in this figure legend, the reader is referred to the web version of this article.)

It should be mentioned that well-crystallized samples (type **I** films), display smaller micro-structural parameter (g_{hkl} and ε_{rms}) and larger (L_{hkl}) than those observed in P3HT spin-coated films, see e.g. Ref. [48], showing a tendency of **P**(**NDI2OD-T2**) backbone towards ordering on the medium range, in spite of long mobile alkylic side-chains.

Moreover the Pseudo-Voigt mixing parameter, defined as the weighted sum of Gauss and Lorentz curves in peak profile description, is calculated to range from 0.58 to 0.68, indicating a prevalent Gaussian character with respect to average values observed by Rivnay et al. [30] for high M_n **P**(**NDI2OD-T2**) and by Prosa et al. [44] for poly(3-didodecylthiophene) **PDDT**. [49]

A relevant features is that the $L_{(001)}$ value (related to backbone extension) is close to overall polymer length for type **I** film (14 nm), while for type **II** and type **III** films such a value is less than half the calculated length ($\leqslant$50 nm). This observation indicates that in low M_n films the backbone assumes a preferentially linear coherent conformation, while for 33 kD films the presence of discontinuities, either meandering [21] or conformational changes, namely ANTI vs SYN -see below- should be inferred.

On the contrary the π–π stacking coherent length, $L_{(020)}$, is very low, rarely exceeding 5–6 nm, indicating severe faults in adjacent backbones, i.e. the intra-lamella mis-match of chains observed by TEM study [21,23], possibly due to partial disorder of branched alkyl chains, clearly frustrating the overall charge transport [20] (see Section 3.4).

The values of Tables 2 and 3 suggest that the reduced polymer length and polydispersity (see Table 1) is beneficial to get deep insight onto crystal structure and orientations.

Specifically in thick films (30–50 nm) the IP and OP profiles yield $d_{(h00)}$ values near to 2.5 nm and to 2.4 nm respectively, clearly indicating a mis-match of lamellae along with the thickness, confirmed by the poor crystallite size along [020] direction – about 4–5 nm –, see Table 2. However for 10 nm films, where a mostly single lamellae is expected to be observed, the observation in many cases of short $L_{(020)}$ has to be ascribed to the above mentioned reasons.

3.3. Orientation and thickness effect

In order to study variation of both order and orientation as a function of depth into the film, 2D images measured at different incidence angles (α_i) are compared. The quantitative evaluation of the orientation according to Baker et al. [50] is in this case prevented due to insufficient amount

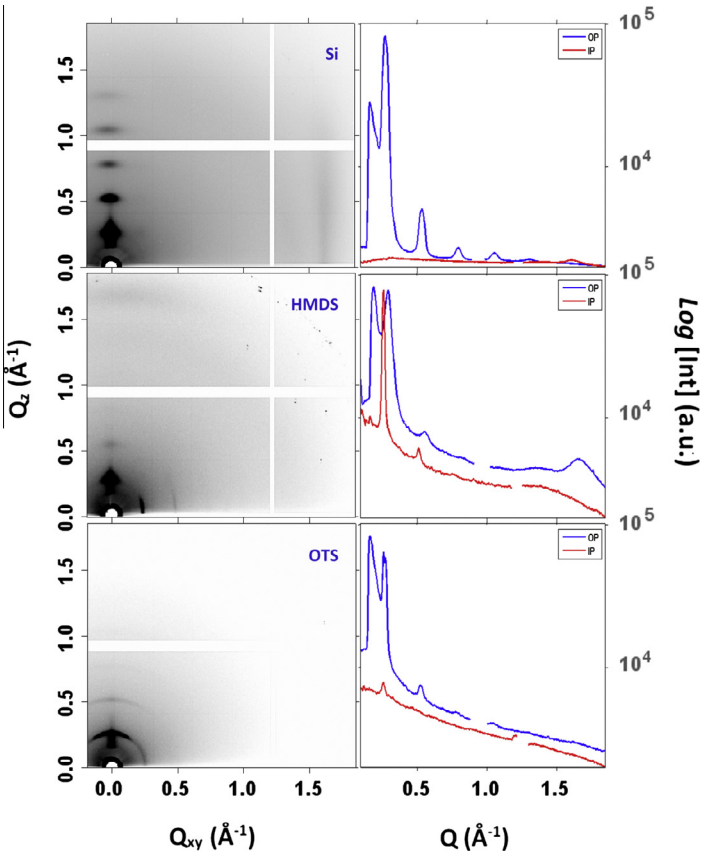

Fig. 3. Two dimensional GIXS measurements of **P(NDI2OD-T2)** type **I** films onto Si, HMDS, and OTS treated at 330 °C recorded at $\alpha_i = 0.2°$. Approximate Q_{xy} and Q_z scales provided to allow comparison with OP-blue- and IP-grey-profiles extracted from the images, properly scaled and shifted for clarity, reported in Q-scale. The X-ray wavelength is 0.12 nm. (For interpretation of the references to color in this figure legend, the reader is referred to the web version of this article.)

of material in diffraction. In fact, considering both the substrate dimension (<0.4 cm^2) and experimental conditions, for complete film penetration [29] the amount of diffracting material is smaller than 10 ng, hence the larger orders of [h00] display too small an intensity in specular reflection conditions. Furthermore the first order suffers from reflectivity tails, hence could not be used for further analysis.

Moreover, even in the case of identically prepared samples examined with the same experimental conditions, significant differences in scattered patterns are observed. Hence to evidence possible fine differences, we resort to comparison of 2D images of the same film at diverse α_i, although with different scattering yield (IP versus OP) – properly corrected for the volume fraction involved in the diffraction – [51]. In this respect we consider the ratio between the areas of pure peaks, i.e. free of reflectivity tails and any overlap with peak belonging to different (hkl). To this end, the ideal choices are (100) in IP and (200) in OP profiles. The relative ratio between the neat areas of two peaks, measured both below ($\alpha_i = 0.05°$ or 0.1°) and above ($\alpha_i = 0.15°$) the critical angle – namely a penetration depth of 5–6 nm and 180 nm respectively [29]-, represent a reliable parameter to map the orientation as a function of depth into the films. In this regard, it should be mentioned that idealizing perfect macromolecule orientation in the film, the ratio should tend towards 0 in case of fully *edge-on* macromolecules and towards ∞ for totally *face-on* macromolecules.

The profile of annealed powders of both **I** and **II** samples, where the orientation of crystallite is generally considered random [52], was taken as reference check, with the ratio between integrated areas of (100) and (200) peaks calculated trough an appropriate background subtraction. Such a ratio consistently ranges between 10.3 and 10.5 according to the slight difference in evaluating background counts [53].

In Table 4, the results of the procedure applied to a series of selected films are reported. The ratio varies both according to the thermal treatment and importantly depth sensitivity. We can effectively note that lower values are *generally* calculated for melt annealed samples (indicating that such films are more *edge-on*), while for the same films increased incidence angle (corresponding to probing deeper into the film) results in a larger ratio. In this respect the occurrence for melt-annealed films of the lamella orientation change (from *face-on* up to *edge-on*) [10,11], is expected to increase the intensity of (h00) in OP with a

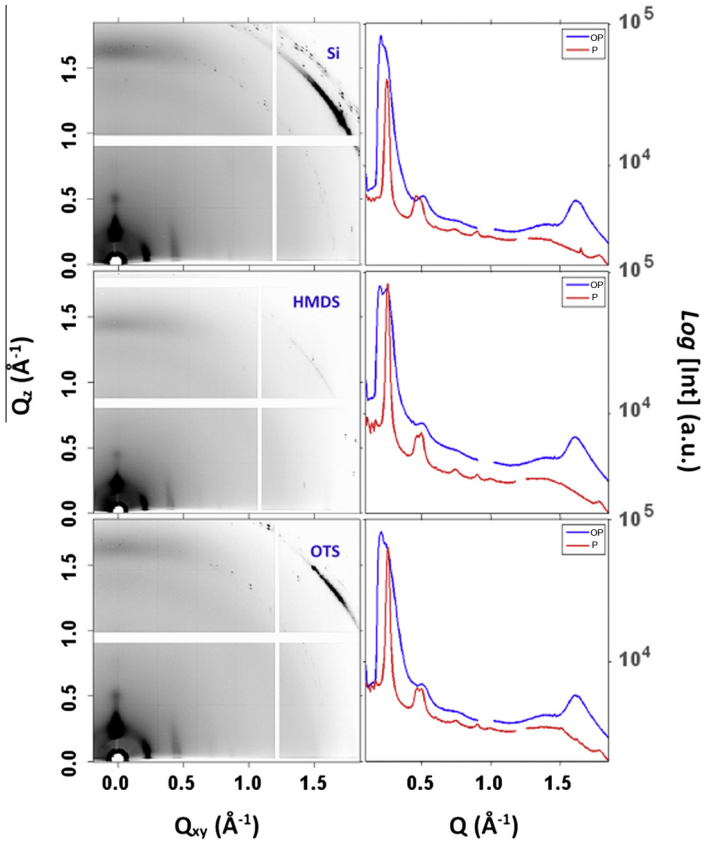

Fig. 4. Two dimensional GIXS measurements of **P(NDI2OD-T2)** type **II** films onto bare Si, HMDS, and OTS treated at 230 °C recorded at $\alpha_i = 0.2°$. Approximate Q_{xy} and Q_z scales provided to allow comparison with OP-blue- and IP-grey-profiles extracted from the images, properly scaled and shifted for clarity, reported in Q-scale. The X-ray wavelength is 0.12 nm. (For interpretation of the references to color in this figure legend, the reader is referred to the web version of this article.)

simultaneous decrease of (h00) in IP. Significantly the top of the film in all samples is consistently found to have more pronounced *edge-on* character.

This orientation change is partially frustrated by silanization effect, i.e. the interaction of both HMDS and OTS with alkyl chains of **P(NDI2OD-T2)**, detailed in Ref. [27]. In fact the annealing time for this samples is doubled with respect to the one necessary for bare SiOx substrates (1 h vs 20 min at 330 °C). Two exemplary cases are indicated in Table 4, **I** OTS with prolonged time of annealing and **I** HMDS, highly speed spin-coated subjected to insufficient thermal treatment time. (Compare lines 2 and 4 with lines 6 and 8 of Table 4). Remarkably the former exhibits complete "lamella flip", while the latter mainly edge-on oriented remains essentially unvaried after annealing.

Although a trend towards lamella flip all along the thickness is indeed observed, especially in type **II** and **III** films; it should be considered that in the grazing conditions the air-exposed layers tend to assume *edge-on* orientation [17], while in the bulk *flat-on* orientation has been evinced [17], therefore the ratio should augment with the penetration depth, as indeed detected and are in agreement with results reported in Ref. [21]. Such a distinct edge-on surface orientation has so far only been evidenced by NEXAFS spectroscopy, so the observation of a different surface orientation with GIWAXS is a significant results and confirms the crystalline nature of this surface layer.

Larger M_n and related polydispersity of type **II** or **III** films cause larger values of the ratio and greater variation according to incidence angle with respect to type **I** samples, possible reasons are below indicated.

The polymer pack in "globuli" either in non solvent or in solvent medium, as evinced in Langmuir–Schäfer film preparation [54] and mostly in a detailed photophysical study [46]. Such a pre-aggregation in solution is stronger for higher M_n samples, due to reduced system solubility [23]. Therefore spin-coating deposition, a non-equilibrium technique where centripetal forces (and shear stress) flatten the macromolecular "globuli" to the substrate [23,46], promotes *face-on* aggregates in films [21].

Conversely lower M_n macromolecules, more solvated in solvent medium, aggregates to a lesser extent, hence are facilitated to form *edge-on* microstructure in spin-coated films.

Indeed polymeric systems, displaying orientation and crystallinity variation along with the thickness, have been observed, particularly for thicker films, and have been attributed to either interaction with the substrate or to a tendency of the polymer to arrange differently from the substrate interface, especially when embedded in

Table 4
Ratios of neat areas of (100) (IP) and (200) (OP) in selected films from 2D images measured at different incident angles (α_i).[a]

Sample[b]	α_i	Ratio[c]
I OTS 230 °C	0.1°	11.1
I OTS 230 °C	0.15°	13.0
I OTS 330 °C	0.05	0.06*
I OTS 330 °C	0.15	0.10*
I HMDS 230 °C	0.05°	2.0
I HMDS 230 °C	0.15°	5.7
I HMDS 330 °C	0.05°	5.0
I HMDS 330 °C	0.15°	6.5
I Si 230 °C	0.15°	11.0
I Si 330 °C	0.15°	0
II HMDS 230 °C	0.05°	10.1
II HMDS 230 °C	0.15°	20.0
II HMDS 330 °C	0.10°	1.2
II HMDS 330 °C	0.15°	2.1
II OTS 230 °C	0.10°	11.4
II OTS 230 °C	0.15°	24.2
II OTS 330 °C	0.10°	0.1
II OTS 330 °C	0.15°	0.2
III Si 230 °C	0.05°	10.0
III Si 230 °C	0.15°	25.0
III Si 330 °C	0.05°	4.1
III Si 330 °C	0.15°	6.0

[a] The integration range in different IP and OP profile was carefully evaluated to yield the comparison homogeneous (see text). Films yielding too weak intensities to give reliable integrated intensities were disregarded.

[b] The three issues indicate the M_n, the film substrate, and the annealing temperature respectively, see text.

[c] The values labeled with asterisk are subject to strong uncertainties. The incidence angle values reported (0.05°, 0.10°, 0.15°) correspond to a penetration depth of 5 nm, 6 nm, 180 nm respectively (see text) to be compared with the film thickness <12 nm, 20 nm, and ~50 nm for **I**, **II**, **III** respectively.

amorphous matrix, so called *bulk effect* [17,26,37,38,40]. In fact type **II** and **III** films, thicker, exhibit markedly such effect, while in type **I** films this trend is weaker (compare also Tables 2 and 3, and previous paragraph).

On the other hand, a variation of the backbone orientation along the thickness is observed even in very crystalline aggregated macromolecules, and different reasons have been put forward according to specific polymeric system under investigation [20]. In this regard films of **P3HT** [39] display long macromolecules, "tie molecules" in fringed micella model [20]; they connect differently oriented lamellae, and at air-interface an orientation change occurs (from *edge-on* to *flat-on*). While films of (poly(2,5-bis(3-tetradecylthiophen-2-yl)thieno[3,2-b]thiophene)) [55] as well of **P**(**NDI2OD-T2**) clearly affected by the drying conditions, show the opposite trend [17], namely from *flat-on* to *edge-on*.

3.4. Phase attribution and packing model

The polymorphic behavior of **P**(**NDI2OD-T2**) identified by Brinkmann et al. [16] in films obtained by epitaxy growth as well as in rubbed films [19], recently confirmed also in regio-regular films [23], has been checked in case of materials having either small M_n or reduced PDI, specifically type **I** and **II** films and powders. In this respect, few indications can be evinced by comparing 2D images of films annealed at 230 °C and 330 °C respectively. The relevant observation is that in case of spin coated and drop- or zone-cast films the intensity ratio between (100) and (200) is largely unbalanced towards first order, differently from what reported in Refs. [16,19] for both the two phases. A possible explanation is the alkyl chain disorder tendency of the **P**(**NDI2OD-T2**) system [21] – i.e. low range order – resulting in a persistently appearance of (100) reflection, at the expenses of the subsequent orders. The observation of no mixed index peaks corroborates the hypothesis of multiple alkyl chains conformations, limiting the order extension. However significant differences in the integrated intensity of (00l) reflections are also observed, possibly indicating a preference to a definite phase in accordance with Brinkmann findings [16,19], see below.

Indeed, Schuettfort et al. [11] and Rivnay et al. [12] reported that thermal annealing over 200 °C provokes not only a dramatic change in morphology but also in structural features, clearly evinced from different peak presence in both IP and OP projections of 2D images, as demonstrated also in above data (see Fig. 3 and already cited Tables). Unfortunately phase ***1*** and ***2*** (according to Brinkmann [16,19]) differ only for small d-spacing variation, making it hard to extract from XRD 2D-images of both films and powders an unambiguous attribution of 3D phases.

In fact the examination of spectra of thermally annealed powders at different temperatures, i.e. 230 °C and 330 °C, for both polymers, M_n = 11 kD or 33 kD, gave essentially the same cell parameters, as shown in Fig. 5; although a contraction of both *a* and *b* axes was observed (as in thin films), specifically $\leqslant$2.45 nm and 0.389 nm were derived from (100) and (020) spacings respectively.

In light of this, we resort to 2D images simulations to provide insight concerning both 3D phase and macromolecule configuration in differently prepared films.

Indeed a detailed study on supramolecular packing compared with 2D simulation appeared recently [24], confirming different configurations of the repeating unit inside the macromolecules [11,21,56], i.e. **T2** and **NDI2OD** moieties can assume **S**, **SA**, and **A** configurations (shown in

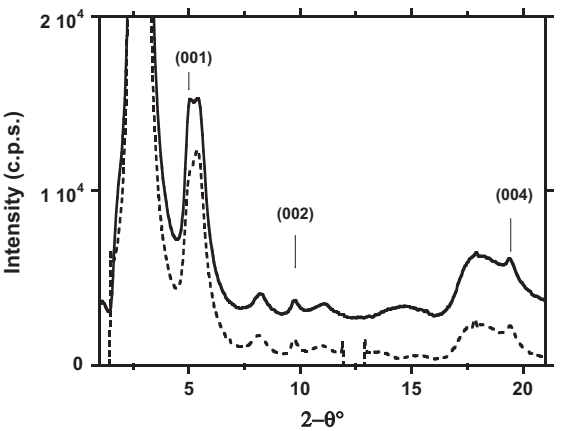

Fig. 5. Comparison of Synchrotron XRD powder spectra of polymer annealed at 230 °C (solid line) and at 330 °C (broken line). The bars indicate [00l] reflections.

Scheme 1). These were evaluated modifying two monomer models calculated by Fazzi [56] from fine ab initio calculations, using MATSTUDIO package [34]. Also the relative calculated energies were similar [21], hence the assumption of presence of all these configurations along with the backbone, especially for larger M_n is reasonable, as well as the coexistence of different configurations along with the macromolecules.

However a clear cut parameter should be considered i.e. the repeating length, which is close to 1.42 nm for **S** and **A** but doubled for **SA** configuration, excepting the possibility of severe in-chain disorder which can modify the macromolecular directionality (e.g. meandering, bending) [21]. This assumption is in striking contrast with the experimental data since in all structural studies so far reported, the present one included, no 2.8 nm spacing could be recognized, hence we are inclined to exclude this possibility especially in type **I** films. However the possibility of the co-presence in the macromolecular backbone of different configurations should be considered [24], originating both the observed short range order and the chain meandering [21], especially for materials with larger M_n.

2D images of type **I** films were chosen in view of short macromolecular length, i.e. low M_n, which hinders chain-folding or meandering formation [21], in fact unexpected match between calculated crystallize size ($L_{[00l]}$ = 12 nm) and macromolecular chain length derived from M_n (~10 units, 14 nm) is observed, see Table 2. Moreover such films displayed both the largest crystallite size and smallest internal disorder along *a* and *b* axes, assuring the maximum range of order for both [h00] and [00l] crystallographic directions (see Table 2).

To produce simulated 2D images Breiby's program [57] was run on CIF files produced with MATSTUDIO [34] in different packing arrangements of two distinct phases [16,19]. The unit cell has been accordingly chosen while the monomer geometry has been supplied by Fazzi [56]. The possibility of co-presence of both **S** and **A** configurations is taken into account in view of poor energy difference. However two different approaches could be considered (i) distinct crystals of each configuration (ii) crystal constituted by mixing **S** and **A**; in view of calculation ease, the former approximation was chosen firstly.

In the absence of any peak attributable to hkl reflection in experimental data, we disregarded the choice of triclinic cell adopted by Lemaur [24] while an arbitrary low crystal symmetry was adopted, (monoclinic $P2_1$). Indeed, neither in films nor in powders could peaks attributable to (010) (d = 0.78 nm) be recognized, while (020) reflection could always be assigned (d = 0.39 nm). In this view after fixing the repeating unit at a value of $b/4$, eight different cases for each phase were considered: namely combining **S** or **A** configuration, two opposite macromolecule directions –labeled normal and reverse, due to non centrosymmetric

Table 5
Comparison among ratio of integrated intensities extracted from simulated and experimental profiles considering crystal in $P2_1$ packing in different cases, namely configuration ANTI-ANTI and SYN–SYN (SS), backbone orientation with respect to b axis, backbone direction, and phase (***1***, ***2***).[a]

Phase 1											Powder annealed at 230 °C
(hkl)	**DO**[b]										
	ANTI–ANTI					SYN–SYN					
	n-NDI[c]	r-NDI	n-T2[c]	r-T2	n-T2[d]	n-NDI	r-NDI	n-T2	r-T2	n-NDI[d]	
(020)	0.170	0.164	0.070	0.095	0.122	0.205	0.180	0.097	0.073	0.256	0.75
(001)	0.880	0.022	0.590	0.640	0.131	2.070	0.930	1.318	0.470	0.486	0.70
(200)	1	1	1	1	1	1	1	1	1	1	1
(300)	0.170	0.164	0.086	0.099	0.134	0.600	0.530	0.333	0.021	0.600	0.16
(400)	0.018	0.020	0.006	0.008	0.011	0.047	0.045	0.024	0.022	0.105	0.08
(500)	0.004	0.003	0.000	0.000	0.0002	0.030	0.036	0.004	0.000	0.047	0.01
(002)	0.001	0.004	0.001	0.000	0.080	0.140	0.079	0.084	0.075	0.114	0.10
(004)	0.009	0.004	0.005	0.006	0.0004	0.001	0.000	0.001	0.001	0.059	0.13
Phase 2											Powder annealed at 330 °C
	ANTI–ANTI					SYN–SYN					
	n-NDI[c]	r-NDI	n-T2	r-T2	n-T2[d]	n-NDI	r-NDI	n-T2	r-T2	n-NDI[d]	
(020)	0.200	0.218	0.108	0.114	0.122	0.210	0.242	0.086	0.129	0.256	0.48
(001)	0.002	0.011	0.124	0.103	0.131	0.100	0.450	0.141	0.437	0.486	0.27
(200)	1	1	1	1	1	1	1	1	1	1	1
(300)	0.190	0.210	0.098	0.127	0.134	0.640	0.680	0.304	0.500	0.600	0.13
(400)	0.020	0.034	0.011	0.010	0.011	0.166	0.102	0.023	0.031	0.105	0.07
(500)	0.004	0.006	0.000	0.000	0.0002	0.045	0.045	0.003	0.013	0.047	0.01
(002)	0.100	0.074	0.073	0.066	0.080	0.029	0.133	0.062	0.069	0.114	0.075
(004)	0.001	0.000	0.001	0.003	0.0004	0.024	0.054	0.023	0.038	0.059	0.12

[a] The ratios are referred to (200) for convenience the backbone direction is different in the assumption of $P2_1$ packing, as a first approximation the peak width has been considered similar for all crystallographic directions, allowing for only a linear increment as a function of 2-theta angle, according to experimental data trend. The backbone orientation is referred to naphtalene-bis(dicarboximide) (NDI) and bithiophene (T2) moieties more flat towards ac plane (substrate film).

[b] DO stands for direction-orientations n = a versus while r = reverse.

[c] NDI and T2 mean naphtalene-bis(dicarboximide) and bithiophene respectively.

[d] Two significant cases of $P22_12$ arrangement are reported to exemplify the improvement of the matching between observed and calculated intensities when in the model is introduced disorder (see text).

space group –, and planarity of **NDI2OD** or **T2** with respect to the substrate (see Fig. 2).

In the calculated models the alkyl chain conformations were considered similarly to those whose energy had been minimized in Ref. [24].

The intensity of the relevant peaks, (h00), (0k0), and (00l) was considered and calculated for both IP and OP profiles. To enable suitable comparison, normalization to (200) reflection was chosen, as the first order is always observed with excessively large intensity, making unfeasible the comparison with any model. In the simulation the peak width was set slightly increasing as a function of 2-θ° value, following the experimental trend. Fixing the torsion angle τ between **NDI2OD** and **T2** moieties close to 46° [56] (see Fig. 1), two possibilities can be considered in model building: macromolecules with **NDI2OD** or with **T2** more *flat-on* in the *ac* plane. Indeed the steric repulsions oblige to conceive situations where neither **NDI2OD** nor **T2** can be really flat; on the other hand long alkyl branched chains can assume a lot of distinct conformations, hence a severe uncertainty occurs.

In Table 4 the integrated intensities of significant reflections normalized to (200) calculated for different models and packings and corresponding integrated intensities of annealed powders, as derived by adequate background subtraction (confirmed by reference to the spectrum of solid polymer cast by pouring methanol into chlorobenzene solution), are reported. The original integrated intensities values are reported in Table S3. A general mis-match is observed between observed and calculated data, hence only on these bases a conclusion could not be achievable, even restricting the analysis to the most intense peaks; however it should be noted that co-presence of both the configurations in the crystal is quite possible in view of the similar calculated energy [21,24,56].

Confirmation of the non-unique configuration comes from the models in $P22_12$ approximation for phase ***2*** reported in Table 5 (columns 5 and 10); in fact considering a crystal constituted by 50% of macromolecules running along a direction and 50% along the opposite one, as a consequence of *crystal static disorder* along with the *c* axis, the sequence of calculated intensities gets closer to the experimental ones. Indeed the limit of this assumption in form of possible multiple side-chain conformations has already been mentioned. In this view the comparison between simulation and experimental data have to be considered qualitative only, due to the quite unfavorable ratio between experimental data and parameters to be optimized.

Moreover the recent study on **NDI2OD** and **T2** moieties conformations with respect to *ac* plane (substrate) [17] allows us to select according to thermal treatment, namely phase ***1*** preferentially **NDI2OD** flat or phase ***2*** preferential **T2** flat. Nevertheless no univocal trend can be achieved unless more situations (backbone direction, **S** versus **A** configuration, and **NDI2OD** versus **T2** orientation) should be properly taken into account. In this frame, taking **S** and **A** configurations, a closer match between Integrated intensities and calculated ones, fixing **NDI2OD** more flat, is found for powders annealed at 230 °C, assuming a phase ***1*** packing, and for the corresponding powders annealed at 330 °C, assuming phase ***2*** arrangement. A further support to this approximation, the [00l] intensity sequence completely follows the literature findings [16,19,23] (see Fig. 5). Namely in phase **1** $I_{(001)} \geqslant I_{(002)} \sim I_{(004)}$, while in phase **2** $I_{(001)} < I_{(002)} \sim I_{(004)}$.

As an example best significant models in the approximation of $P2_1$ space group are drawn using MATSTUDIO package [34] and shown in Fig. 6: **A** configuration in phase ***1*** (top) with $a = 2.48$, $b = 0.79$, $c = 1.410$ nm, and $\beta = 90°$; and **S** in phase ***2*** (bottom) with $a = 2.45$, $b = 0.79$, $c = 1.418$ nm, and $\beta = 99°$.

Since the simulated 2D images are clearly more crowded compared with the experimental ones; (see Fig. S5 in Supplementary data), we resorted to consider only the calculated reflections clearly recognized in the experimental 2D data in order to simplify the reader view. Indeed it should be considered the chemical constitution of this polymer system i.e. layers of rigid backbones separated by flexible alkyl side chains, leads to unregistered stacking of two-dimensional sheets, suggesting non unique conformation of side alkyls, as already detected in semi-rigid macromolecular systems such as poly(9,9-dioctylfluorenyl-co-bithiophene) [58] and, to a lesser extent, poly(9,9-di-*n*-octylfluorene-*alt*-benzothiadiazole) [40].

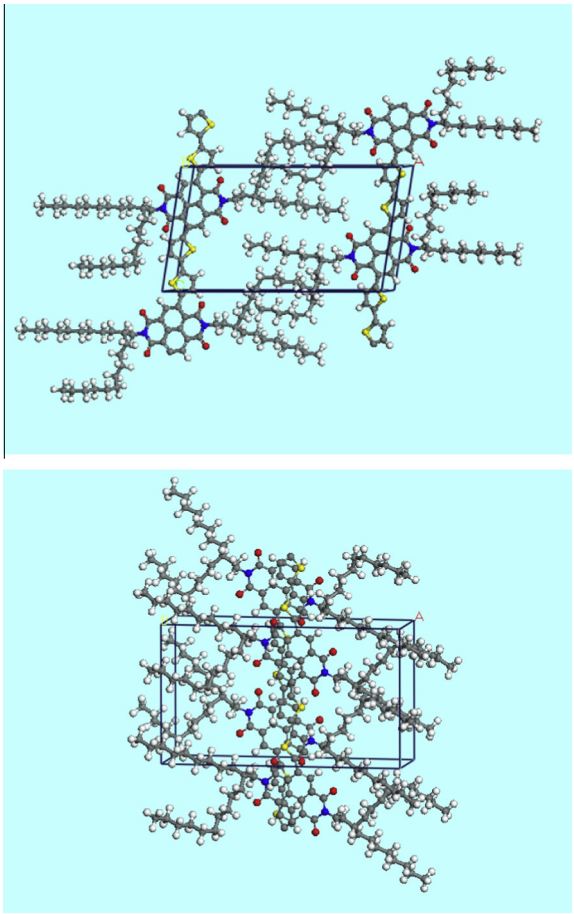

Fig. 6. Models of crystal packing in $P2_1$ space group approximation, as derived from MATSTUDIO of **P**(**NDI2OD-T2**) in ANTI-ANTI (top) and SYN-SYN (bottom) configurations for phase ***1*** and ***2*** respectively.

Moreover the co-presence of intra-lamella **A** and **S** macromolecules promptly account for unregistered adjacent polymeric layers, due to differently positioned alkyl chains. If long range order could be reached, profiles from best crystallized type **I** films should display most of (hkl) peaks detected by Brinkmann [16,19], as the peak overlap has been ruled out for both phase **1** and phase **2**, by choosing appropriate experimental conditions (see Supplementary data). As a matter of fact, only in films obtained by either epitaxy growth [16] or rubbing procedure [19], properly annealed, hkl reflections were observed, confirming a reduced lateral order in such a complex polymer.

In Fig. 7 a comparison of experimental and simulated 2D images is presented. IP and OP profiles from powders, films, and simulations are also compared. The clear Bragg rods in the simulated 2D images – see second and fourth images on the top of Fig. 7 –, less evident in the corresponding experimental ones, are due to "perfect crystal approximation" in Breiby's program [59].

In the middle and bottom parts of Fig. 7, profiles of powder samples (blue trace) are compared with experimental IP (orange trace), simulated IP (black trace), experimental OP (red trace), and simulated OP (green trace) for phase ***1***, in the $P2_1$ **A** model, and for phase ***2***, in the $P22_12$ **S**

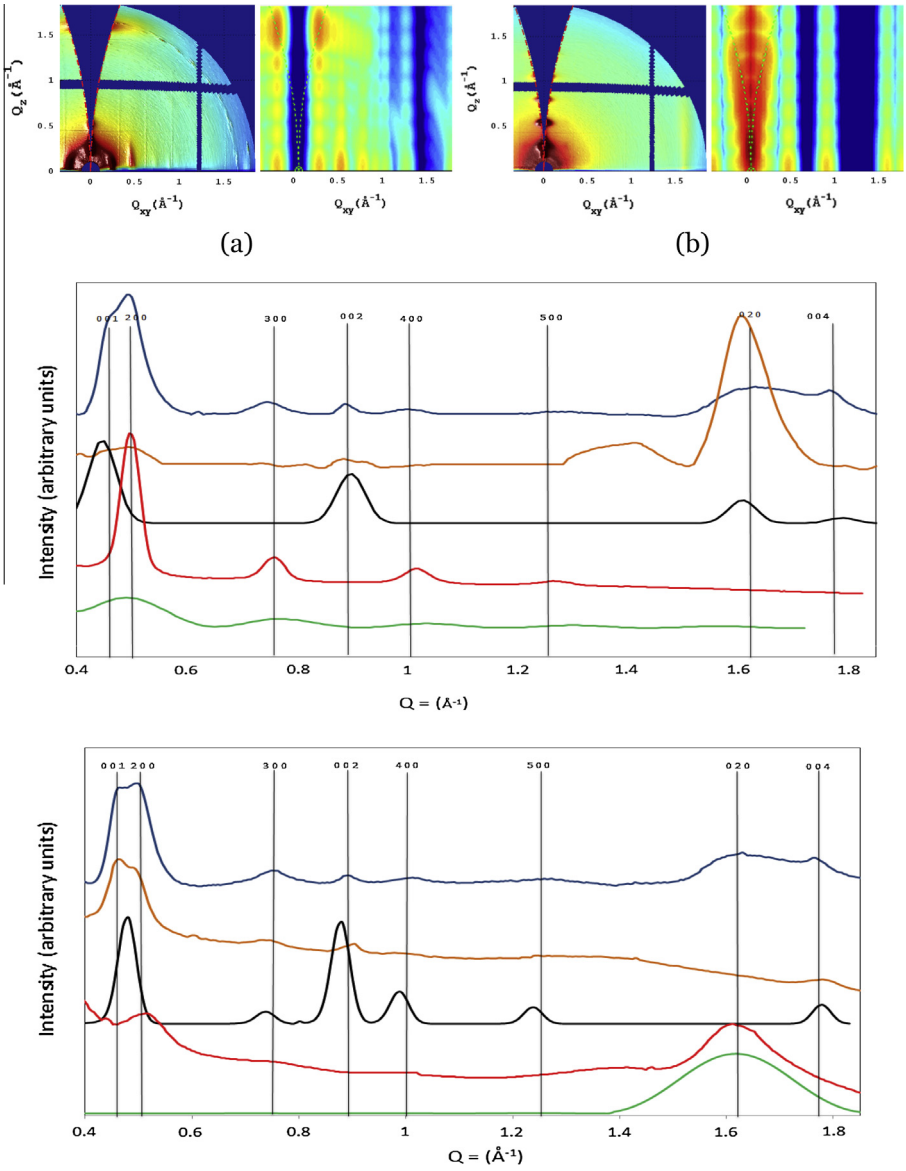

Fig. 7. 2D images experimental (exp) -left- and simulated (sim) -right- as referred to as phase ***1***(annealed at 230 °C) (a) and to phase ***2***(annealed at 330 °C) (b). Sim 2D are oriented along [0 2 0] (a) and [1 0 0] (b) respectively. Comparison of powder profiles and OP and IP profiles extracted from corresponding exp 2D a, b with profiles from simulated 2D; phase ***1***(top), phase ***2*** (bottom): powders (blue), exp IP (orange), sim IP (black), exp OP (red) and sim OP (green). The bars indicated q values of considered reflections based of simulated unit cell, which can slightly differ from the experimental ones (see text). The peak with asterisk is due to SiO_x diffraction. (For interpretation of the references to color in this figure legend, the reader is referred to the web version of this article.)

model. The orientation [020] and [100] were assumed for phase ***1*** and ***2*** respectively, as derived by intensity trend of (00l) reflections (see above). A right trend of peak intensities is evidenced for both the two phases.

Remarkably, this approach is intended to indicate an approximate packing in the crystal of both phases in the complex case of co-presence of distinct configurations (**S**, **A**) in the film, while the presence of mixed situations, i.e. **SA** configuration or errors in each one (a **S** in **A**-chain or viceversa) is disregarded in view of the backbone length (near to 10 monomers), realistically preventing either bending or meandering.

4. Conclusions

Through a careful synchrotron investigations on thin film (12–50 nm thick) of semi-rigid **P**(**NDI2OD-T2**), evidence of fine differences among polymer samples having various M_n and PDI has been found. Utilizing grazing incidence diffraction with varied depth sensitivity, differences in both crystal size and perfection [25] along with the thickness of the film have been presented, demonstrating the high crystallinity of the film although confined to short range.

In well crystallized low M_n films, evidence of closer packing (compared to the 30 kD and larger polydispersed samples) is clear, together with a greater crystal size and reduced intra-crystalline disorder according to Hosemann [42], resembling those observable in epitaxially grown films [16].

Concerning the crystallite orientation with respect to the substrate, some dispersed orientation of the lamella is evidenced by the persistent presence of (100) peak. Examining the relative amount of IP and OP lamellar scattering, we have found direct evidence for increased *edge-on* character at the polymer/air interface as previous detected by NEXAFS spectroscopy.

Of the three possible backbone configurations, shown in Scheme 1, the ANTI–SYN should be ruled out in view of anomalous main-chain repetition, 2.8 nm, never being experimentally observed. While the other two should be taken into account, due to small energy difference [24]; the present data does not enable distinction between the two.

Simulation of 2D patterns, based on the two phases proposed by Brinkmann [16] and considered in pseudo monoclinic arrangement, ($P2_1$) indicated a huge number of peaks as compared with any film pattern, clearly confirming a lack of long range order, possibly due to multiple conformations of branched side-chains. A good match between the observed powder data and simulated profiles could also not be achieved, even considering *crystal static disorder* in the $P22_12$ approximation, because of possible co-crystallisation of ANTI–ANTI and SYN–SYN configurations.

Experimental patterns of films annealed at 230 °C and of films annealed at 330 °C best match phases ***1*** and ***2*** respectively, assuming the proper orientation, i.e. (020) and (100) respectively, with the 2D simulated according to Breiby's approach [57]. A complex mis-matching between simulated and experimental profiles is observed, indicating co-presence of different situations in crystalline part of the film, i.e. **S** or **A** configurations, backbone direction, and **NDI2OD** versus **T2** orientation [24].

On the other hand the results of the present paper represent a strong confirmation of the suggestions indicated by Dunitz [60], i.e. the relevance of entropic contribution in crystal packing.

Acknowledgements

Thanks are due to prof. A. Facchetti for supplying polymer of different molecular weights and helpful suggestions, to prof. D.W. Breiby for giving us his program SIMDIFF, and also to dr. D. Fazzi for giving the initial monomer geometry *SYN* and *ANTI* to build up the crystal and to simulate 2D diffraction images. This research was undertaken in part on the soft X-ray beamline at the Australian Synchrotron, Australia. [61] CRM acknowledges support from the Australian Research Council (FT100100275) and thanks Dr. Lars Thomsen of the Australian Synchrotron for technical support.

Appendix A. Supplementary material

Supplementary data associated with this article can be found, in the online version, at http://dx.doi.org/10.1016/j.eurpolymj.2014.10.005.

References

[1] Wang C, Dong H, Hu W, Liu Y, Zhu D. Semiconducting π-conjugated systems in field-effect transistors: a material odyssey of organic electronics. Chem Rev 2012;112:2208–67.
[2] Baeg K, Khim D, Jung S, Kang M, You I, Kim D, et al. Remarkable enhancement of hole transport in top-gated N-type polymer field-effect transistors by a high-k dielectric for Ambipolar electronic circuits. Adv Mater 2012;24:5433–9.
[3] Guo X, Kim FS, Seger MJ, Jenekhe SA, Watson MD. Naphthalene Diimide-based polymer semiconductors: synthesis, structure-property correlations, and n-channel and Ambipolar field-effect transistors. Chem Mater 2012;24:1434–42.
[4] Baeg K, Jung S, Khim D, Kim J, Kim D, Koo JB, et al. Low-voltage, high speed inkjet-printed flexible complementary polymer electronic circuits. Org Electr 2013;14:1407–18.
[5] Beaujuge PM, Fréchet JMJ. Molecular design and ordering effects in π-functional materials for transistor and solar cell applications. J Am Chem Soc 2011;133:20009–29.
[6] Liang Y, Yu L. A new class of semiconducting polymers for bulk Heterojunction solar cells with exceptionally high performance. Acc Chem Res 2010;43:1227–36.
[7] Wang E, Hou L, Wang Z, Hellström S, Zhang F, Inganäs O, et al. An easily synthesized blue polymer for high-performance polymer solar cells. Adv Mater 2010;22:5240–4.
[8] Yan H, Chen Z, Zheng Y, Newman C, Quinn JR, Dötz F, et al. A high-mobility electron-transporting polymer for printed transistors. Nature 2009;457:679–86.
[9] Durban MM, Kazarinoff PD, Luscombe CK. Synthesis and characterization of thiophene-containing naphthalene diimide n-type copolymers for OFET applications. Macromolecules 2010;43:6348–52.
[10] Rivnay J, Toney MF, Zheng Y, Kauvar IV, Chen Z, Wagner V, et al. Unconventional face-on texture and exceptional in-plane order of a high mobility n-type polymer. Adv Mater 2010;22:4359–63.
[11] Schuettfort T, Huettner S, Lilliu S, Macdonald JE, Thomsen L, McNeill CR. Surface and bulk structural characterization of a high-mobility electron-transporting polymer. Macromolecules 2011;44:1530–9.
[12] Rivnay J, Steyrleuthner R, Jimison LH, Casadei A, Chen Z, Toney MF, et al. Drastic control of texture in a high performance n-type polymeric semiconductor and implications for charge transport. Macromolecules 2011;44:5246–55.

[13] Facchetti A. Polymer donor–polymer acceptor (all-polymer) solar cells. Mater Today 2013;16:123–32.
[14] Schubert M, Dolfen D, Frisch J, Roland S, Steyrleuthner R, Stiller B, et al. Influence of aggregation on the performance of all-polymer solar cells containing low-bandgap naphthalenediimide copolymers. Adv Energy Mater 2012;2:369–80.
[15] Mori D, Benten H, Okada I, Ohkita H, Ito S. Low-bandgap donor/acceptor polymer blend solar cells with efficiency exceeding 4%. Adv Energy Mater 2014;4. 1301006 (1–6).
[16] Brinkmann M, Gonthier E, Bogen S, Tremel K, Ludwigs S, Hufnagel M, et al. Segregated versus mixed interchain stacking in highly oriented films of naphthalene diimide bithiophene copolymers. ACS Nano 2012;6:10319–26.
[17] Schuettfort T, Thomsen L, McNeill CR. Observation of a distinct surface molecular orientation in films of a high mobility conjugated polymer. J Am Chem Soc 2013;135:1092–101.
[18] Fabiano S, Yoshida H, Chen Z, Facchetti A, Loi MA. Orientation-dependent electronic structures and charge transport mechanisms in ultrathin polymeric n-channel field-effect transistors. Appl Mater Interface 2013;5:4417–22.
[19] Tremel K, Fischer FSU, Kayunkid N, Di Pietro R, Tkachov R, Kiriy A, et al. Charge transport anisotropy in highly oriented thin films of the acceptor polymer P(NDI2OD-T2). Adv Energy Mater 2014;4. 1301659 (1–13).
[20] Noriega R, Rivnay J, Vanderwal K, Koch FPV, Stingelin N, Smith P, et al. A general relationship between disorder, aggregation and charge transport in conjugated polymers. Nature Mater 2013;12:1038–44.
[21] Takacs CJ, Treat ND, Krämer S, Chen Z, Facchetti A, Chabinyc ML, et al. Remarkable order of a high-performance polymer. Nano Letters 2013;13:2522–7.
[22] Tanase C, Meijer EJ, Blom PWM, de Leeuw DM. Local charge carrier mobility in disordered organic field-effect transistors. Org Electron 2003;4:33–7.
[23] Steyrleuthner R, Di Pietro R, Collins BA, Polzer F, Himmelberger S, Schubert M, et al. The role of regioregularity, crystallinity, and chain orientation on electron transport in a high-mobility n-type copolymer. J Am Chem Soc 2014;136:4245–56.
[24] Lemaur V, Muccioli L, Zannoni C, Beljonne D, Lazzaroni R, Cornil J, et al. On the supramolecular packing of high electron mobility naphthalene Diimide copolymers: the perfect registry of asymmetric branched alkyl side chains. Macromolecules 2013;46:8171–8.
[25] Dimitrakopoulos CD, Malenfant PRL. Organic thin film transistors for large area electronics. Adv Mater 2002;14:99–117.
[26] Fazzi D, Caironi M, Castiglioni C. Quantum-chemical insights into the prediction of charge transport parameters for a naphthalenetetracarboxydiimide-based copolymer with enhanced electron mobility. J Am Chem Soc 2011;133:19056–65.
[27] Porzio W, Scavia G, Barba L, Arrighetti G, Milita S. Depth-resolved molecular structure and orientation of polymer thin films by synchrotron X-ray diffraction. Eur Polymer J 2011;47:273–83.
[28] Senkovskyy V, Tkachov R, Komber H, John A, Sommer J, Kiriy A. Mechanistic insight into catalyst-transfer polymerization of unusual anion-radical naphthalene diimide monomers: an observation of Ni(0) intermediates. Macromolecules 2012;45:7770–7.
[29] Dosch H, Battermann BW, Wack DC. Depth-controlled grazing-incidence diffraction of Sinchrotron X-radiation. Phys Rev Lett 1986;56:1144–7.
[30] Rivnay J, Noriega R, Kline RJ, Salleo A, Toney MF. Quantitative analysis of lattice disorder and crystallite size in organic semiconductor thin films. Phys Rev B 2011;84. 045203 (1–20).
[31] Gozzo F, De Caro L, Giannini C, Guagliardi A, Schmitt B, Prodi A. The instrumental resolution function of synchrotron radiation powder diffractometers in the presence of focusing optics. J Appl Cryst 2006;39:347–57.
[32] Hammersley AP, Svensson SO, Hanfland M, Fitch AN, Hausermannm D. Two-dimensional detector software: from real detector to idealised image or two-theta scan. High Press Res 1996;14:235–48.
[33] Roisnel T, Rodriguez-Carvajal J. WinPLOTR: a windows tool for powder diffraction pattern analysis. Mater Sci Forum 2001;378–381:118–23.
[34] MATSTUDIO modeling release 4.0, Accelrys Inc. 9685 Scranton Rd. San Diego CA (USA); 2003. <www.accelrys.com>.
[35] Stöhr J. In "NEXAFS Spectroscopy". Springer: Berlin; 1992.
[36] Brinkmann M. Structure and morphology control in thin films of regioregular poly(3-hexylthiophene). J Polymer Sci Part B: Polymer Phys 2011;49:1218–33.
[37] Kohn P, Rong Z, Scherer KH, Sepe A, Sommer M, Müller-Buschbaum P, et al. Crystallization-induced 10-nm structure formation in P3HT/PCBM blends. Macromolecules 2013;46:4002–13.
[38] Factor BJ, Russell TP, Toney MF. Grazing incidence X-ray scattering studies of thin films of an aromatic polyimide. Macromolecules 1993;26:2847–59.
[39] McNeill CR, Ade HJ. Soft X-ray characterisation of organic semiconductor films. J Mater Chem C 2013;1:187–201.
[40] Rapallo A, Barba L, Arrighetti G, Scavia G, Porzio W, McNeill CR, et al. Unpublished results.
[41] Chabinyc ML, Toney MF, Kline RJ, Heeney I, McCulloch M. X-ray scattering study of thin films of poly(2,5-bis(3-alkylthiophen-2-yl)thieno[3,2-b]thiophene). J Am Chem Soc 2007;129:3226–37.
[42] Hindeleh AM, Hosemann R. Microparacrystals – the intermediate stage between crystalline and amorphous. J Mater Sci 1991;19:5127–36. and ref. therein.
[43] Lilliu S, Agostinelli T, Pires E, Hampton M, Nelson J, Macdonald JE. Macromolecules 2011;44:2725–34.
[44] Prosa TJ, Moulton J, Heeger AJ, Winokur MJ. X-ray structural studies of poly(3-alkylthiophenes): an example of an inverse comb. Macromolecules 1999;32:4000–9.
[45] Rivnay J, Mannsfeld SCB, Miller CE, Salleo A, Toney MF. Quantitative determination of organic semiconductor microstructure from the molecular to device scale. Chem Rev 2012;112:5488–519.
[46] Steyrleuthner R, Schubert M, Howard IA, Klaumünzer B, Schilling K, Chen Z, et al. Aggregation in a high-mobility n-type low-bandgap copolymer with implications on semicrystalline morphology. J Am Chem Soc 2012;134:18303–17.
[47] As usually adopted, the unit cell axes a, b, and c point along the side-chains, the π-stacking direction and the polymer backbone, respectively.
[48] Scavia G, Barba L, Arrighetti G, Milita S, Porzio W. Structure and morphology optimization of poly(3-hexylthiophene) thin films onto silanized silicon oxide. Eur Polymer J 2012;48:1050–61.
[49] These Pseudo-Voigt parameter values imply, also in the Hosemann approximation, a comparable contribution to the peak shape of both g_{hkl} and ε_{rms} parameters, as expected from a polymeric system constituted by a large rigid core and mobile long alkyl chains, surely stiffer than PDDT.
[50] Baker JL, Jimison LH, Mannsfeld S, Volkman S, Yin S, Subramanian V, et al. Quantification of thin film crystallographic orientation using X-ray diffraction with an area detector. Langmuir 2010;26:9146–51.
[51] Birckholz M. In "Thin Film Analysis by X-Ray Scattering" Weinheim WILEY-VCH Verlag GmbH & Co. KGaA; 2006.
[52] see e.g. Klug HP, Alexander LE. In X-ray diffraction procedures for polycrystalline and amorphous materials. New York: John Wiley & Sons; 1974.
[53] With regard to the integration range in 2D images of both IP and OP profiles, typical ranges adopted were 170–176° in IP, in order to avoid any possible masking effect of the beam-stop, and 85–95° in OP profiles respectively. Specifically arcs including intensities significantly over the background, were considered. In order to make the comparison homogeneous, arcs of the same amplitude were used in the integration process for all the films.
[54] Fabiano S, Musumeci C, Chen Z, Scandurra A, Wang H, Loo Y, et al. From monolayer to multilayer N-channel polymeric field-effect transistors with precise conformational order. Adv Mater 2012;24:951–6.
[55] Schuettfort T, Watts B, Thomsen L, Lee M, Sirringhaus H, McNeill CR. Microstructure of polycrystalline PBTTT films: domain mapping and structure formation ACS. NANO 2012;6:1849–64.
[56] Giussani E, Fazzi D, Brambilla L, Caironi M, Castiglioni C. Molecular level investigation of the film structure of a high electron mobility copolymer via vibrational spectroscopy. Macromolecules 2013;46:2658–70.
[57] Breiby DW, Bunk O, Andreasen JW, Lemked HT, Nielsen MM. Simulating X-ray diffraction of textured films. J Appl Cryst 2008;41:262–71.
[58] Werzer O, Resel R, Chernev B, Plank H, Rothmann MM, Strohriegl P, et al. Crystallographic structure and morphology of bithiophene-fluorene polymer nanocrystals. Polymer 2011;2:3368–73.
[59] Stein GE, Knoll W, Advincula RC, editors. In functional polymer films: 2 volume set. Wiley-VCH; 2012. p. 669–94 [chapter 20].
[60] Brock CP, Dunitz JD. Chem Mater 1994;6:1118–27.
[61] Cowie BCC, Tadich A, Thomsen L. The current performance of the wide range (90–2500 eV) soft X-ray Beamline at the Australian synchrotron. In: AIP conf proc 1234; 2010. p. 307–10.